




Control of stoichiometry and morphology in polycrystalline V_2O_3 thin films using oxygen buffers

Jonathan A. J. Rupp^{1,*} , Benoît Corraze³, Marie-Paule Besland³, Laurent Cario³, Julien Tranchant³, Dirk J. Wouters¹, Rainer Waser^{1,2}, and Etienne Janod³

¹RWTH, Aachen, Germany

²PGI-7 FZ, Jülich, Germany

³Institut des Matériaux Jean Rouxel (IMN), CNRS, Université de Nantes, Nantes, France

Received: 6 March 2020

Accepted: 28 June 2020

Published online:

17 July 2020

© Springer Science+Business Media, LLC, part of Springer Nature 2020

ABSTRACT

In this work, we investigate the influence of low temperature reduction conditions (873 K) by different oxygen buffers on the off-stoichiometry of polycrystalline V_2O_3 thin films. Vanadium oxide thin films (thickness 300 nm and 100 nm) have been grown by reactive sputtering and have been annealed in a buffered atmosphere subsequently. Buffer couples were chosen throughout the stability range of $V_{2-y}O_3$ ($y \leq 0.03$) by the use of different oxygen buffer combinations, namely Ni/NiO, Fe/Fe₃O₄, Cr/Cr₂O₃ and Mn/MnO. Thin films have been characterized by scanning electron microscopy, X-ray diffractometry and low temperature electrical transport measurements. Upon decreasing the oxygen partial pressure, the mean grain size of V_2O_3 decreases systematically from 45 ± 20 nm with a high porosity to 27 ± 10 nm without porosity. The most favourable reduction conditions have been identified for Fe- and Cr-based couples. Moreover, all thin films reduced by the four buffer couples exhibit high insulator-to-metal transition temperatures (110–155 K) close to the value of ideally stoichiometric $V_{2-y}O_3$ ($y < 0.005$) (155 K) as well as large changes in resistance at the transition (three to five orders of magnitude). This oxygen buffer method hence provides a valuable synthesis method of highly stoichiometric polycrystalline V_2O_3 thin films with technological relevance.

Introduction

The binary system of vanadium and oxygen consists of various Magnéli (V_nO_{2n-1}) and Wadsley (V_nO_{2n+1}) phases [1]. Most of these phases show remarkable electronic and magnetic phase transitions [2]. Amongst them, corundum-type V_2O_3 undergoes an

insulator-to-metal transition (IMT) at 155 K. This transition occurs between an antiferromagnetic (insulating) monoclinic phase at low temperature and a paramagnetic (conducting) rhombohedral corundum phase at high temperature [3]. Upon decreasing temperature, the phase change is accompanied by a drop of the c/a ratio as well as an increase in volume

Address correspondence to E-mail: rupp@iwe.RWTH-Aachen.de

of about 1.2% [4]. At room temperature, substituting vanadium with more than 1.1 at.% chromium induces a transition from paramagnetic metal to paramagnetic Mott insulator while retaining the same corundum structure [4]. Applying physical pressure on $(V_{1-x}Cr_x)_2O_3$ leads to the inverse IMT and restores the metallic state [4]. More interestingly, the Mott insulator-to-metal transition can not only be driven by pressure or temperature [4] but also by an electric field [5]. Therefore, this archetype Mott–Hubbard insulator is of strong interest for application in resistively switching devices [6] and neuromorphic circuits [7, 8]. However, very accurate control of stoichiometry is required to achieve a well-defined Mott-insulating state that matches the required half-filling criteria [9, 10]. Such a control of the vanadium–oxygen ratio is crucial in thin films on which electrical applications will be based. For instance, deviations of stoichiometry in $V_{2-y}O_3$ as low as $y = 0.03$ indeed lead to an absence of the low temperature IMT [11]. Various synthesis methods are used to obtain phases with low oxygen content. Only non-equilibrium synthesis methods can provide a direct deposition approach which has to be performed under very low oxygen partial pressure, e.g. molecular beam epitaxy, electron beam evaporation or reactive sputtering [12]. A direct deposition method therefore also requires very precise and simultaneous control of various deposition parameters, e.g. sputtering power and process pressure. In contrast, equilibrium synthesis relies on a two-step approach with deposition of a phase with higher oxygen content and subsequent reduction under thermodynamic control. For this method, the magnitude of synthesis parameters can be simplified with two remaining parameters of oxygen atmosphere and process temperature. The oxygen content is controlled by reducing atmospheres such as CO/CO₂ or Ar/H₂ [11], usually at high temperatures above 1000 K. For instance, Shivashankar et al. [11] investigated the vanadium defect concentration of non-stoichiometric $V_{2-y}O_3$ single crystals. Controlled formation of the latter across the pure-phase window of V_2O_3 has been achieved at a reduction temperature of 1473 K in CO/CO₂ atmosphere. Single crystals with controlled non-stoichiometry have been synthesized by annealing in atmospheres with different CO/CO₂ ratios and subsequent quenching. With this approach, a huge reduction of the vanadium point defect density (decreasing y from 0.02 down to 0.007)

with a concomitant increase in transition temperature from 10 to 155 K could be achieved by lowering the oxygen partial pressure towards the equilibrium line of VO/V₂O₃. An equivalent method to control the oxygen partial pressure can be achieved by oxygen buffers [11] that similarly imposes an oxygen partial pressure with a metal–metal oxide buffer couple (see experimental part). Here, we show that reduction with an oxygen buffer can be successfully applied to control the stoichiometry of polycrystalline V_2O_3 thin films even for low annealing temperatures such as 873 K. Four different buffer couples (BC) have been chosen to aim at four different stoichiometry values in the range of phase-pure V_2O_3 . Based on thermochemical data [13], one might expect that the vanadium vacancies y in $V_{2-y}O_3$ decrease with the BC's according to $y_{Ni-NiO} > y_{Fe-Fe_3O_4} > y_{Cr-Cr_2O_3} > y_{Mn-MnO}$. On the contrary, we found that for thin films, reduction annealing with the mentioned oxygen buffers does not follow the thermodynamic principle of single crystals reduced at high temperatures anymore.

Experimental

A promising method to provide very precise control over point defects in a thin film is to exploit the thermodynamic equilibrium of a reaction between a metal-oxide combination. Each dynamic equilibrium between a metal and its corresponding oxide is defined by its Gibbs free energy ΔG that consists of an enthalpy ΔH and entropy ΔS terms. In this case, referring to the Ellingham approximation, both are considered temperature independent. The change in ΔG can then be related to the oxygen partial pressure $p(O_2)$ in a direct way:

$$\Delta G = \Delta H - T\Delta S = -RT \ln p(O_2) \quad (1)$$

where R denotes the gas constant, T the temperature and $p(O_2)$ the oxygen partial pressure in thermodynamic equilibrium between the two solids. With given reaction enthalpies and entropies from literature (Table 1), the equilibrium oxygen partial pressure was straightforwardly calculated for four different oxygen buffer associations within the window of off-stoichiometric V_2O_3 . Amorphous vanadium oxide thin films (thickness 300 nm and 100 nm) have been deposited on silica by RF-reactive sputtering from a one-inch vanadium target. The oxygen

Table 1 Quantity of metal and oxide powder used for annealing of layers with the four BC combinations. Enthalpy ΔH and entropy ΔS extracted from Reed et al. [13]

Reaction equation	Metal mass (mg)	Oxide mass (mg)	ΔH (kJ/mol)	ΔS (J/K/mol)
$2\text{Ni} + \text{O}_2 \leftrightarrow 2\text{NiO}$	158 (78.6)	200 (100)	- 474.43	167.2
$\frac{3}{2}\text{Fe} + \text{O}_2 \leftrightarrow \frac{1}{2}\text{Fe}_3\text{O}_4$	145 (72.4)	200 (100)	- 543.40	153.0
$\frac{4}{3}\text{Cr} + \text{O}_2 \leftrightarrow \frac{2}{3}\text{Cr}_2\text{O}_3$	136.8 (68.4)	200 (100)	- 744.04	167.2
$2\text{Mn} + \text{O}_2 \leftrightarrow 2\text{MnO}$	140 (64.5)	190 (100)	- 767.03	148.0

partial pressure $p(\text{O}_2)$ was adjusted by the flux ratio of two mass flow controllers: one with pure argon (90 sccm) and one with a mixture of argon and oxygen in the ratio 99:1 (10 sccm). This allowed control of the $p(\text{O}_2)$ in a 10^{-6} – 10^{-4} mbar range. The relatively low oxygen partial pressure value of 10^{-5} mbar for deposition was used to reach a V:O ratio close to 2:3 in the amorphous films prior to reducing annealing (where the measured average value constituted 2:4 [14]). The used power of $P = 50$ W and the process pressure of $p = 10^{-2}$ mbar resulted in a deposition rate of $q = 3.3$ nm/min. Thin films were subsequently placed inside silica tubes with a metal and oxide powder couple at a pressure of $p < 10^{-3}$ mbar to provide a constant V:O stoichiometry ratio independent of temperature. After sealing, the tubes were annealed in a tubular furnace at a temperature of 873 K, with a heating rate of 300 K/h, an annealing time of 1 h at 873 K, and finally passive free cooling down to room temperature with a rate of ~ 100 K/h. Figure 1 displays the theoretical equilibrium oxygen partial pressures for the four selected buffer couple reactions between metals and oxides with respect to temperature. Buffer couples were chosen to introduce an increasing concentration of vanadium defects as a result of an increase in oxygen partial pressure from Mn-based to Cr-/Fe-/Ni-based BCs. Metal and oxide quantities were weighted according to the reaction equation's mole masses. Morphology was determined by scanning electron microscopy (SEM) images with a Zeiss "DSM982 GEMINI" microscope. Lateral grain sizes were determined by the line section method, meaning that the amount of intersecting grain boundaries has been counted along several horizontal lines of SEM images and have been divided by the length of the investigated section. Surface vacancy area (100 nm layers) and surface crack area (300 nm layers) were determined by ImageJ 1.51d with a contrast filter. X-ray diffraction (XRD) patterns were recorded in Bragg–Brentano geometry with a Bruker X-ray diffractometer. Lattice parameters were extracted by le Bail refinement with

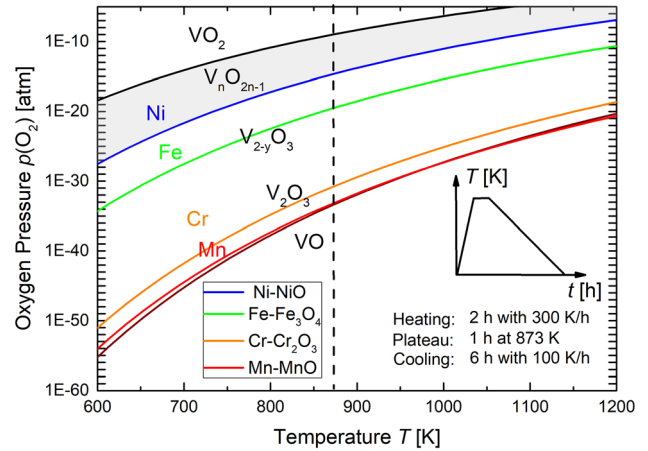


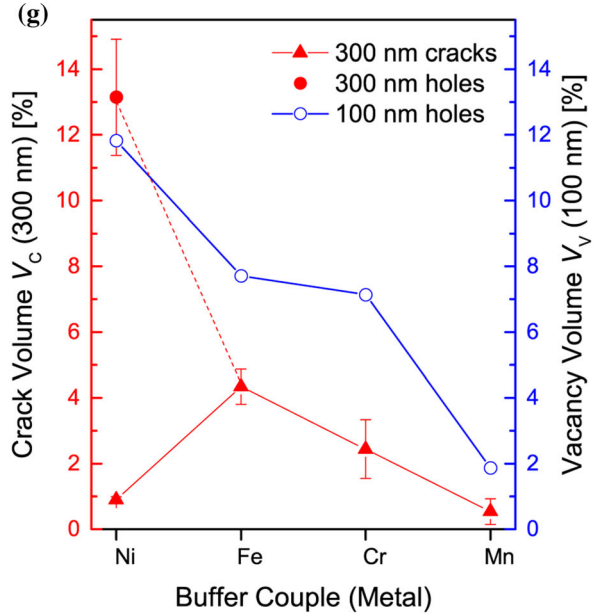
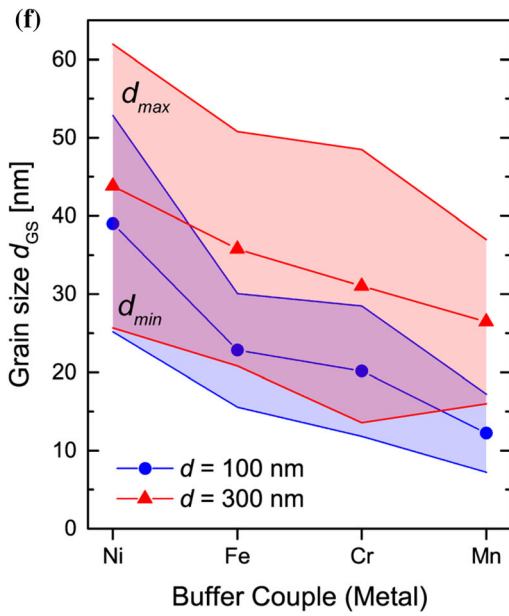
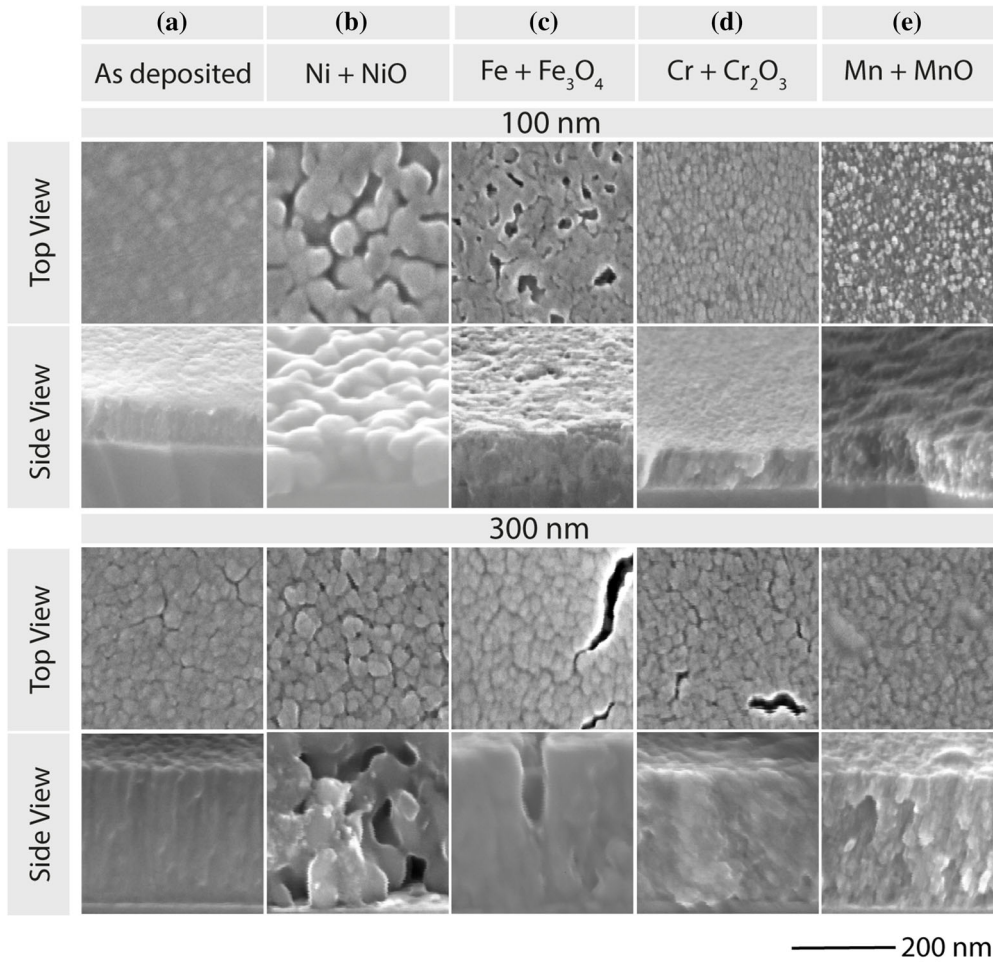
Figure 1 Equilibrium oxygen partial pressures $p(\text{O}_2)$ associated to of the different oxygen buffer couples as function of annealing temperature. Calculations based on Ellingham diagram [13] (compare Table 1). Dashed line describes maximum reduction temperature used in this work. Inset: sketch of the annealing procedure.

JANA software from XRD patterns. To investigate electrical transport characteristics at low temperatures in four-point configuration, a closed-cycle helium circuit cryostat "Omniplex DE210" from ARS was used. Transition temperatures of the IMT were determined for the cooling and heating branch at the turning point of the derivative logarithmic resistance versus inverse temperature ($d(\ln R)/d(1/T)$).

Results

Morphology

Figure 2 presents morphological changes of V_2O_3 thin films throughout the stoichiometry window. As-deposited amorphous 100 nm thin films already present a rough surface with relatively large particles up to 36 nm in diameter (Fig. 2a top), whereas 300 nm thick films show a relatively dense columnar structure (Fig. 2a bottom). The 100 nm thick film annealed with BC Ni/NiO exhibits a grain size of



◀ **Figure 2** SEM images (top and side view) for 100 nm thin and 300 nm thick V_2O_3 films on silica substrates for pristine amorphous layers (a) and layers after annealing with different buffer couples: Ni + NiO (b), Fe + Fe_3O_4 (c), Cr + Cr_2O_3 (d), Mn + MnO (e). **f** Lateral grain size d_{GS} for 100 nm (blue circles) and 300 nm (red triangles) V_2O_3 thin films with grain size distribution. **g** Evolution of vacancy volume V_V (blue circles) and surface crack area V_C (red triangles) for 100 nm and 300 nm V_2O_3 thin films with error bars.

$d_{Ni,100} = 39 \pm 14$ nm with visible surface pinholes (Fig. 2b top). The grain size is comparable to the pristine amorphous state (Fig. 2a top). For 300 nm (Fig. 2b bottom), grain size increases slightly ($d_{Ni,300} = 44 \pm 18$ nm) compared to 100 nm thick thin films and the cross section image shows a more porous bulk morphology (Fig. 2b bottom) as compared to the pristine amorphous dense columnar structure (Fig. 2a bottom). For BC Fe/ Fe_3O_4 (Fig. 2c top) and a thickness of 100 nm, grain size ($d_{Fe,100} = 23 \pm 7$ nm) as well as pinhole size decreases compared to Ni/NiO, quantitatively described by Fig. 2f, g. With respect to the 100 nm films reduced by Fe/ Fe_3O_4 , an increased grain size is obtained for 300 nm ($d_{Fe,300} = 36 \pm 15$ nm) thick layers (Fig. 2c bottom). In addition, a considerable part of the surface is covered with formed cracks. Layers synthesized with a BC Cr/ Cr_2O_3 (Fig. 2d top) show a smaller average grain size ($d_{Cr,100} = 20 \pm 8$ nm) with few smaller pinholes for 100 nm layers as compared to 100 nm thick layers annealed with BC Fe/ Fe_3O_4 (Fig. 2c top). Corresponding 300 nm thick layers (Fig. 2d bottom) still form cracks to a lesser extent compared to BC Fe/ Fe_3O_4 (Fig. 2c bottom) and present only a slightly higher grain size than 100 nm layers ($d_{Cr,300} = 23 \pm 7$ nm). Lastly, BC Mn/MnO (Fig. 2e top) results in a very fine grain size of ($d_{Mn,100} = 15 \pm 2$ nm) with a considerably higher roughness compared to BC Cr/ Cr_2O_3 which is reflected by a spatial variation in contrast. For 300 nm layers (Fig. 2e bottom), a flatter surface with increased grain size is visible compared to 100 nm thin films ($d_{Mn,300} = 26 \pm 10$ nm). Yet, in this case, broad hills grow on the surface (instead of cracks as found for BCs Fe/ Fe_3O_4 and Cr/ Cr_2O_3). Table 2 summarizes average lateral grain sizes d_{GS} with distributions of 100 nm thin and 300 nm thick vanadium oxide films. To sum up, grain sizes (Fig. 2f) and free volume (Fig. 2g) in form of surface cracks or void volume

(represented by the quantified free area) decrease equally with the chosen sequence of buffer couples.

Crystal structure and lattice parameters

All films were characterized by XRD analysis (Fig. 3a) where diffraction patterns of 300 nm thick films show the typical lattice planes of corundum V_2O_3 [15]. XRD records from 100 nm thick films exhibit diffraction peaks with weak intensity, not suitable to accurately resolve lattice parameters. Thus, cell parameters were extracted from XRD patterns obtained for 300 nm thick V_2O_3 thin films. For the V_2O_3 thin film obtained by buffer couple Ni–NiO, black arrows denote an (unknown) formed secondary phase. Table 3 summarizes the obtained lattice parameter values and fitting parameters where the goodness of fit (GOF) as a measure for the quality of the fit (between 1.03 and 1.20) is close to its ideal value (1.0). In Fig. 3b, the variation of unit cell parameters as function of BC type is plotted (where bulk V_2O_3 values are indicated by horizontal lines). For all buffer couples, the c/a ratios (orange star) deviate from the bulk value except for Mn/MnO where the c/a ratio matches the ideal c/a ratio of V_2O_3 . Furthermore, with BC Ni/NiO for off-stoichiometric $V_{2-y}O_3$, c -parameter (green triangle) and cell volume (blue hexagon) are compressed by 0.05 \AA and 1 \AA^3 , respectively, whereas the a -parameter (red square) is slightly expanded by 0.01 \AA . With BC to lower $p(O_2)$ (left to right in Fig. 3b), c -parameter and cell volume relax to bulk values whereas the a -parameter expands even more up to the BC Cr– Cr_2O_3 . For BC Mn/MnO, parameters a and c as well as the cell volume are reduced compared to bulk. Due to internal strain with a change of the unit cell volume and the a -parameter, an increase in the IMT temperature is expected from BC Ni–NiO to Cr– Cr_2O_3 and a decrease for BC Mn–MnO.

Electrical transport characteristics

With low temperature electrical transport measurements, the insulator-to-metal transition of V_2O_3 was investigated for 300 nm thick films (Fig. 4a) as well as 100 nm thick films (Fig. 4b). For all buffer couple combinations, both thicknesses exhibit similar trends with sharp transition behaviour as well as an increase in room temperature resistivity towards the equilibrium line of V_2O_3/VO , indicating a high

Table 2 Average lateral grain size d_{GS} for 100 nm with standard deviations, surface crack area V_C and vacancy volume V_V for 100 nm and 300 nm V_2O_3 thin films with error bars

Buffer couple	Ni–NiO	Fe–Fe ₃ O ₄	Cr–Cr ₂ O ₃	Mn–MnO
d_{GS} ($d = 100$ nm) (nm)	39 ± 14	23 ± 7	20 ± 8	15 ± 2
d_{GS} ($d = 300$ nm) (nm)	44 ± 18	36 ± 15	23 ± 7	26 ± 10
V_V ($d = 100$ nm) (%)	11.8	7.7	7.1	1.9
V_C ($d = 300$ nm) (%)	13.1 ± 1.8	4.3 ± 0.5	2.4 ± 0.9	0.5 ± 0.4

For 300 nm thin films reduced with BC Ni–NiO, porosity is denoted as void volume V_V since there were no cracks on the sample surface

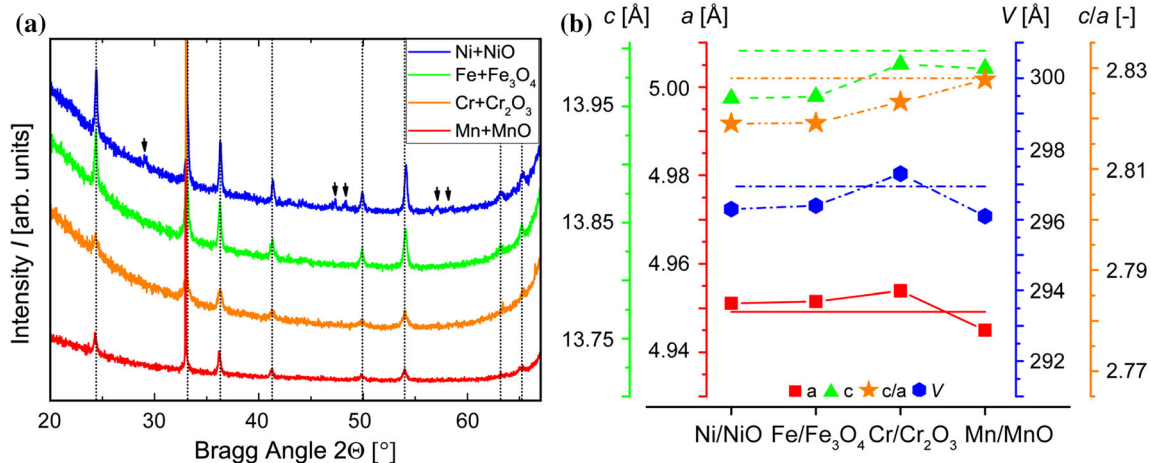


Figure 3 **a** X-ray diffraction patterns in Bragg–Brentano geometry for 300 nm thick V_2O_3 films. All thin films exhibit a corundum $R\bar{3}c$ structure corresponding to V_2O_3 lattice planes [15] (vertical dashed lines) with an unknown secondary phase indicated

by black arrows. **b** Unit cell parameters of 300 nm thick V_2O_3 films after annealing process with different buffer couples: c -parameter (green), a -parameter (red), cell volume V (blue), c/a ratio (orange). Horizontal lines correspond to bulk values [4].

Table 3 Le Bail fitting parameters for 300 nm thick films with buffer couple type BC, reliability factors R_p , weighted reliability factors wR_p , goodness of fit GOF, cell

BC	R_p (%)	wR_p (%)	GOF	a (Å)	c (Å)	c/a (Å)	V (Å ³)
Ni + NiO	4.93	6.66	1.18	4.9511	13.9570	2.8190	296.3
Fe + Fe ₃ O ₄	4.96	6.63	1.20	4.9515	13.9587	2.8191	296.4
Cr + Cr ₂ O ₃	4.54	5.97	1.03	4.9539	13.9865	2.8233	297.3
Mn + MnO	4.70	6.14	1.03	4.9450	13.9828	2.8277	296.1

reproducibility of the reduction process in this thickness range. The lowest transition temperatures between 90 and 140 K were found for the two extreme BC's, namely Mn–MnO and Ni–NiO. Besides, Fe–Fe₃O₄ and Cr–Cr₂O₃ revealed the highest transition temperatures between 110 and 157 K. In the case of a 300 nm thick V_2O_3 film annealed with BC Fe–Fe₃O₄, the largest resistance change is observed with five to six orders of magnitude, in good agreement with the transition magnitude obtained for single crystals [4]. In these experiments, 300 nm thick films exhibit a slightly broader hysteresis than the 100 nm ones. While varying the nature of the BC, room temperature resistivity increases continuously by roughly one order of magnitude

from $4.7 \cdot 10^{-4} \Omega \text{ cm}$ (300 nm Ni/NiO) to $3.0 \cdot 10^{-3} \Omega \text{ cm}$ (300 nm Mn/MnO). To be able to identify the differences between reduction processes in the transition region in more detail, the negative differential resistance versus inverse temperature is plotted as a function of temperature (Fig. 4c). Interestingly, one can identify two maxima for each branch in the 300 nm thick film reduced by BC Ni + NiO (blue plot) and even three maxima for the two samples reduced by BC Fe + Fe₃O₄ (green plot). Generally, for each thickness, one would expect only one maximum for cooling as well as heating owing the hysteresis linked to the first-order transition, as found for BCs Cr + Cr₂O₃ and Mn + MnO. Figure 4d summarizes the development of transition

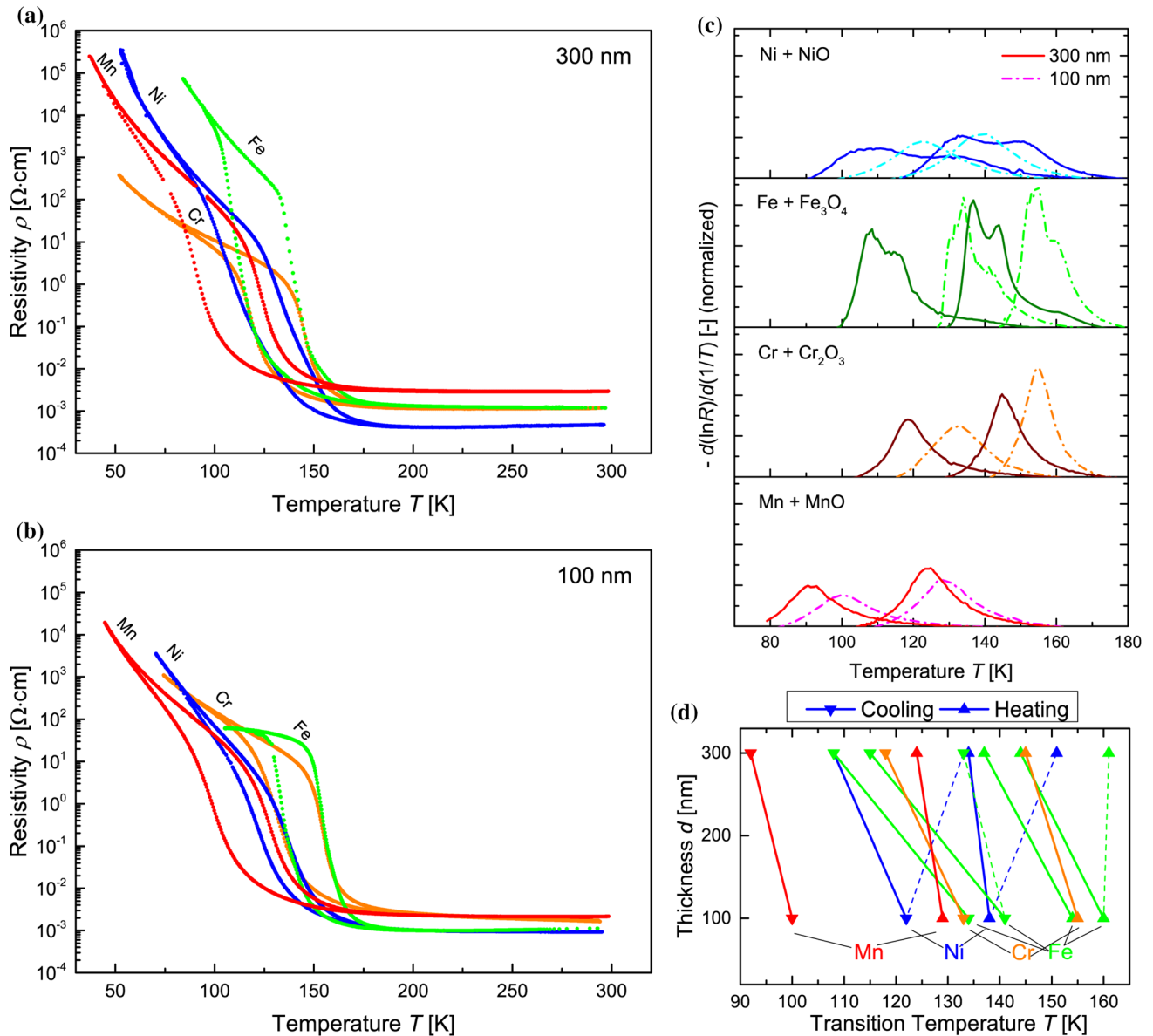


Figure 4 **a, b** Low temperature electrical transport characteristics of annealed V_2O_3 thin films for both thicknesses **a** 300 nm, **b** 100 nm reduced with the four buffer couples: Ni + NiO (blue), Fe + Fe_3O_4 (green), Cr + Cr_2O_3 (orange), Mn + MnO (red). **c** Derivative of logarithmic resistance versus inverse temperature for the four used buffer couples and two vanadium oxide

thicknesses of 300 nm and 100 nm. **d** Transition temperatures of cooling (triangles facing down) and heating (triangles facing up) branch for the four buffer couples and two thicknesses. Dashed lines describe additional transition temperatures in more complex derivatives of Ni&Fe-based BCs (compare **c**).

temperatures for used buffer couples and thicknesses. Lower thicknesses of 100 nm exhibit higher transition temperatures with an increase between 5 and 25 K with respect to the 300 nm one. An increasing transition temperature can be found in the case of Mn, Ni to Fe and Cr, with split transition temperatures into multiple maxima for Fe and Ni.

Discussion

In the following sections, the deviation of our results from ideal thermodynamic principles are interpreted in more detail for each oxygen buffer couple individually and are summarized in the last section.

Buffer couple Ni–NiO

XRD patterns of 300 nm thick thin films (Fig. 3a) confirm a corundum-type V_2O_3 structure with a small fraction of an unknown secondary phase. Thermodynamically, the most stable phase in ambient atmosphere after completion of the reduction process would be VO_2 [16] on large time scales and oxides with comparable stoichiometry belonging to the Magnéli phases V_nO_{2n-1} such as V_6O_{11} [17]; those phases differ only by a change in sheared crystallographic planes [17]. The exposure to air after reduction might lead to surface oxidation and an appearance of V_2O_3 grains exhibiting a shell constituted of oxide phases close to $VO_{x \sim 2}$ (e.g. V_6O_{11})—as has already been detected in the case of epitaxially grown V_2O_3 [18, 19]. Indeed, the high porosity (as observed in SEM images in Fig. 2b, g marked as “300 nm holes”) can further promote surface oxidation more deeply within the “bulk” thin film with a larger surface area exposed to air. Low temperature electrical transport measurements (Fig. 4a) reveal a broad transition temperature range between 100 and 165 K for 300 nm thick films with two sharp slope maxima (visible in the derivative of the resistance in Fig. 4c dark blue) which could also be explained by a possible formation of an additional V_6O_{11} phase with a bulk transition temperature of its IMT of 177 K [20]). In combination with the V_2O_3 transition temperature at 155 K [4], two maxima would be formed separated by a temperature shift of 22 K. Here, we observe a variation of 18 K and 25 K, for cooling and heating curve, respectively. Since the c/a ratio is lower than the bulk value (Fig. 3b) (which should be constant if related only to the deviation in vanadium deficiency [21]), one can conclude that internal stress is present in the thin film. Therefore, the shift of both transition temperatures of V_2O_3 and V_6O_{11} compared to bulk values could be related to a compressive stress within the film as revealed by the compressed cell volume (Fig. 3b). In contrast, for 100 nm thin films (Fig. 4b), only a single slope maximum is present (Fig. 4c light blue) which indicates a transition of a pure V_2O_3 phase for this thickness.

The fact that an (almost) ideal stoichiometric V_2O_3 phase with a quite high transition temperature can be synthesized with BC Ni–NiO (inducing a relatively high oxygen partial pressure) is rather surprising since thermodynamics would predict a highly non-stoichiometric thin film with a transition temperature

close to 10 K [11]. Like many other binary metal oxides, NiO is known to provide a non-stoichiometry regime that changes with temperature [22]. Therefore, this effect may shift the iso-composition line towards more reducing conditions during the annealing process. Apparently, the deviation towards reducing conditions that occurs during the iso-compositional cooling process with BC Ni–NiO favours a nearly stoichiometric V_2O_3 phase (in contrast to a quenching process of single crystals after the use of high reduction temperatures [11]). Consequently, one could also relate the two maxima in transition slope to a change in BC conditions with a stoichiometric NiO phase at the maximum reduction temperature (belonging to the lower maximum) and a final $Ni_{1-3x}^{2+}Ni_{2x}^{3+}O$ phase at room temperature (belonging to the higher maximum). However, no change in colour of the BC could be observed after the reduction process, i.e. from green colour of a stoichiometric NiO towards grey/black colour of a non-stoichiometric compound. Moreover, this explanation would need to rely on strongly deviating reduction conditions between the two thicknesses since no peak splitting was observed for the thinner film (100 nm) reduced by BC Ni/NiO.

Buffer couple Fe–Fe₃O₄

The smaller grain size obtained with BC Fe–Fe₃O₄ at lower oxygen partial pressure compared to Ni–NiO (Table 2, Fig. 2c) is likely to be a side effect of stronger out-diffusion of oxygen from the initially amorphous film. The stronger excorporation of oxygen could favour the nucleation density during crystallization which may hinder grain growth and recrystallization in the reduction process. Cell parameters are similar to those obtained with BC Ni–NiO with compressed values except for a slight tensile strained as revealed by the a -parameter value (Fig. 3b). However, the resistance jump observed at transition is roughly one order of magnitude higher for 300 nm thick films (five orders of magnitude instead of four orders of magnitude for BC Ni/NiO, Fig. 4b) and the transition itself shows three maxima in slope (Fig. 4c). A possible explanation for this slight dispersion of the transition temperature is an inhomogeneous distribution of vanadium vacancies γ within grains of the $V_{2-\gamma}O_3$ phase. This would happen if the trajectory of the $p(O_2)$ –temperature imposed by the Fe–Fe₃O₄ couple (indicated by the green line in

Fig. 1) does not strictly correspond to a constant y value in $V_{2-y}O_3$. As a consequence, a gradient between the grain core and its shell would arise during the cooling part of the annealing process (see inset in Fig. 1), which can be “frozen” at low temperature as soon as the kinetics of vanadium diffusion becomes too slow. Such a core–shell gradient in vanadium vacancies y could therefore easily explain the distribution of transition temperature shown in Fig. 4c. Moreover, this scenario is consistent with the different transition temperatures observed in 100 nm and 300 nm thick films annealed with Fe–Fe₃O₄, since their strongly different grain sizes (23 nm for the 100 nm thick film, against 37 nm for the 300 nm thick one, Table 2) could lead to a different final distribution of vanadium vacancies within each grain.

Buffer couple Cr–Cr₂O₃

In contrast to all other BCs, the cell volume is expanded and the c -parameter only exhibits a slight compression. Thus, one expects the transition temperature to be raised which is confirmed for 300 nm thick films (147 K in Fig. 4a). In analogy, 100 nm thick films exhibit a transition temperature similar to Fe–Fe₃O₄ (Fig. 4b). However, the resistivity jump at transition is reduced by over one order of magnitude. Apparently, the quite dense nanostructure with small crystallites (average size < 20 nm, Table 2) might not be sufficient to provide the required space of 1% free volume that is necessary to enable the volume expansion of the low temperature phase transition [4]. Only surface-related grains might provide enough free volume close to cracks and pinholes (Fig. 2g). For both thicknesses of 100 nm and 300 nm, a sharp single maximum of the transition slope is present (Fig. 4c) which resembles a pure and dense corundum V₂O₃ phase as well as a uniform distribution of stress. The very controlled conditions are likely to be a consequence of the Cr–O phase diagram where only pure Cr₂O₃ is a thermodynamically stable phase [23]. Lacking intermediate phases thus prevents any shift of the iso-composition line.

Buffer couple Mn–MnO

An obvious difference of 100 nm thick films reduced by BC Mn–MnO is an increased roughness (Fig. 2e1) and a highly dense thin film with smallest grain diameters of ~ 12 nm. In contrast to the previously

discussed BCs, 300 nm thick films do not exhibit any cracks or pinholes in surface. Instead, hill growth is visible at the surface. Grain sizes and “void” volume drop to the minimum for both thicknesses compared to all other BCs. XRD analysis confirms the presence of a pure V₂O₃ phase belonging to $R\bar{3}c$ type (Fig. 2a) where diffraction peaks are significantly broadened and fully coherent with a small grain size of 26 ± 10 nm. Compared to stoichiometric bulk V₂O₃, this film displays the same c/a ratio, but a lower unit cell volume, i.e. a compressive internal stress. According to Ref. [21], this could indicate an “oxygen non-stoichiometry”: $z = 0.044$ in the (erroneous) formulation V₂O_{3+z}, or rather to vanadium deficiency $y = 0.029$ in the correct V_{2-y}O₃ description (Fig. 2b). This would lead to a transition temperature as low as 10 K and thus a metallic behaviour [11]. Obviously, this scenario is not coherent with the observed transition temperature above 100 K and the resistivity jump at transition of three to four orders of magnitude, respectively (Fig. 4a, b). A possible explanation could be the extreme reducing conditions imposed by the Mn–MnO buffer couple leading to oxygen vacancies and an effective composition V₂O_{3-x} ($x > 0$). As for the case of well-established vanadium vacancies in V_{2-y}O₃, such oxygen vacancies would lead to the reduction of the unit cell volume, without changing the c/a ratio, as we observed experimentally.

Comparison of oxygen buffer couples

Clearly, the existence of simple vanadium deficiencies V_{2-y}O₃ initially proposed in “ideal” single crystals with high temperature reduction [11] is insufficient to explain the behaviour of all our thin films obtained with low temperature reduction. The four oxygen buffer combinations investigated in this study allowed obtaining thin films very close to ideal stoichiometric V₂O₃, as evidenced by a resistance ratio at the IMT higher than four orders of magnitude and by high transition temperatures above 90 K (Fig. 4a, b). Fe- and Cr-base BCs resulted in the highest IMT temperatures of reduced thin films for all investigated BCs close to the ideal value of 150 K. In more detail, various effects such as compressive stress, defect gradients, secondary phase formation as well as morphological differences might be responsible for the specific shapes of transitions of different BCs with multiple maxima in slopes (Fig. 4c, d).

These deviations might partially result from changing stoichiometries of specific buffer couples itself during the annealing process which leads to deviations in reduction conditions from the ideal iso-composition lines (Fig. 1). The morphological differences in form of free volume (Fig. 2g) can be expected to have an impact on nonvolatile resistive switching of Cr-doped V_2O_3 devices as well since a transition of Mott-metallic to Mott-insulating phase requires an increase in cell volume of about 1% [24]. Therefore, thin films reduced by Ni- and Fe-based BCs would provide sufficient free volume for nonvolatile resistive switching where Cr- and Mn-based BCs could hinder the volume expansion by their dense small-grained microstructure. Apart from the presented buffer couples, another oxide–oxide combination Ce_2O_3 – CeO_2 was used for reduction experiments (not shown) where the equilibrium line of oxygen partial pressure lies between the reduction conditions of Fe- and Cr-based BCs. Even though unknown CeO_x phases were formed in the BC after the annealing process (which, again, speaks for the change of BC stoichiometry during reduction), comparable electrical transport properties were obtained with an IMT temperature of 100 K and a resistance jump of five orders of magnitude. Generally, one also has to note that for low temperature reduction, the calculated oxygen partial pressure along the cooling path is below any countable static oxygen partial pressures during the cooling process. Our results thus raise the need for further theoretical investigations of these technologically relevant synthesis conditions for thin films, especially due to the astonishing broad success of the method with various combinations of oxygen buffers.

Conclusion

The absence of point defects as well as the microstructure and stress state of V_2O_3 thin films is of great importance to generate a true Mott-insulating state in Cr-doped (or tensile strained) V_2O_3 thin films for electrical devices. Therefore, polycrystalline V_2O_3 thin films (thickness 300 nm and 100 nm) have been synthesized under controlled thermodynamic conditions at low temperatures and strongly deviate from high temperature reduction experiments on single crystals. Changing the Gibbs free energy by different buffer couples affected morphological features and

resulted in comparable electrical properties. Oxygen buffers close to the equilibrium line of VO/ V_2O_3 (Mn–MnO) and V_2O_3 / V_3O_5 (Ni–NiO) induced a possible oxygen deficiency and secondary phase precipitation, respectively. By lowering of the Gibbs free energy with different oxygen buffers, grain sizes and void regions shrink which is explained by a stronger removal of oxygen during the reduction process. Finally, the Fe– Fe_3O_4 and Cr– Cr_2O_3 oxygen buffers led to the strongest changes in resistance at the IMT's up to five orders of magnitude and highest transition temperatures close to the one of highly stoichiometric V_2O_3 . 100 nm thick films exhibited identical trends with slightly reduced hysteresis width, higher transition temperature and a smaller change of resistance at the transition. These results may have a strong impact on design rules for the miniaturization of resistive Mott-switching devices towards their physical limits.

Acknowledgements

J. A. J. Rupp would like to thank M. Querré and T. Hennen for fruitful discussions. Low temperature electrical transport measurements as well as X-ray diffraction experiments have been performed at the Insitute des Matériaux (IMN Nantes/FR). Furthermore, J. A. J. Rupp greatly acknowledges the Deutsche Forschungsgemeinschaft DFG for funding this project in the Sonderforschungsbereich (SFB) 917.

Compliance with ethical standards

Conflict of interest The authors declare no conflict of interests.

References

- [1] Wriedt HA (1989) The O–V (oxygen vanadium) system. Bull Alloy Phase Diagr 10:271. <https://doi.org/10.1007/BF02877512>
- [2] Stefanovich G, Pergament A, Stefanovich D (2000) Electrical switching and Mott transition in VO_2 . J Phys: Condens Matter 12:8837. <https://doi.org/10.1088/0953-8984/12/41/310>
- [3] Word RE, Werner SA, Yelon WB (1981) Spin waves in vanadium sesquioxide V_2O_3 . J Phys Rev B 23:3533. <https://doi.org/10.1103/PhysRevB.23.3533>

- [4] McWhan DB, Rice TM, Remeika JP (1970) Metal-insulator transition in $(V_{1-x}Cr_x)_2O_3$. *Phys Rev Lett* 23:1384. <https://doi.org/10.1103/PhysRevB.2.3734>
- [5] Stoliar P, Cario L, Janod E, Corraze B, Guillot-Deudon C, Salmon-Bourmand S, Guiot V, Tranchant J, Rozenberg M (2013) Universal electric field-driven resistive transition in narrow-gap Mott insulators. *Adv Mater* 25:23. <https://doi.org/10.1002/adma.201301113>
- [6] Querré M, Janod E, Cario L, Tranchant J, Corraze B, Bouquet V, Deputier S, Cordier S, Guilloux-Viry M, Besland M-P (2015) Metal-insulator transitions in $(V_{1-x}Cr_x)_2O_3$ thin films deposited by reactive direct current magnetron co-sputtering. *Thin Solid Films* 617:56–62. <https://doi.org/10.1016/j.tsf.2015.12.043>
- [7] Stoliar P, Tranchant J, Corraze B, Janod E, Besland M-P, Tesler F, Rozenberg M, Cario L (2017) A leaky-integrate-and-fire neuron analog realized with a Mott insulator. *Adv Funct Mater* 1604740:1. <https://doi.org/10.1002/adfm.201604740>
- [8] Adda C, Corraze B, Stoliar P, Diener P, Tranchant J, Filatre-Furcate A, Fourmigué M, Lorcy D, Besland M-P, Janod E, Cario L (2018) Mott insulators: a large class of materials for leaky integrate and fire (LIF) artificial neuron. *J Appl Phys* 124:152124. <https://doi.org/10.1063/1.5042756>
- [9] Janod E, Tranchant J, Corraze B, Querre M, Stoliar P, Rozenberg M, Cren T, Roditchev D, Phuoc VT, Besland M-P (2015) Resistive switching in Mott insulators and correlated systems. *Adv Funct Mater* 25:6287. <https://doi.org/10.1002/adfm.201500823>
- [10] Yee C-H, Balents L (2015) Phase separation in doped Mott insulators. *Phys Rev X* 5:021007. <https://doi.org/10.1103/PhysRevX.5.021007>
- [11] Shivashankar SA, Aragon R, Harrison HR, Sandberg CJ, Honig JM (1981) Preparation and electrical properties of V_2O_3 single crystals of controlled stoichiometry. *J Electrochem Soc* 128:2472. <https://doi.org/10.1149/1.2127272>
- [12] Rupp JAJ, Janod E, Besland M-P, Corraze B, Kindsmüller A, Querré M, Tranchant J, Cario L, Dittmann R, Waser R, Wouters DJ (2020) Competition between V_2O_3 phases deposited by one-step reactive sputtering process on polycrystalline conducting electrode. *Thin Solid Films* 705:138063. <https://doi.org/10.1016/j.tsf.2020.138063>
- [13] Reed Thomas B (1971) Free energy of formation of binary compounds. MIT Press, Cambridge
- [14] Rupp JAJ, Querré M, Kindsmüller A, Besland M-P, Janod E, Dittmann R, Waser R, Wouters D (2018) Different threshold and bipolar resistive switching mechanisms in reactively sputtered amorphous undoped and Cr-doped vanadium oxide thin films. *J Appl Phys* 123:044502. <https://doi.org/10.1063/1.5006145>
- [15] Morris MC, McMurdie HF, Evans EH, Paretzkin B, Parker HS (1983) ICDD 00-034-0187 (V_2O_3). *Natl Bur Stand (US) Monogr* 20:108
- [16] Andersson S, Jahnberg L (1963) Crystal structure studies on the homologous series Ti_nO_{2n-1} , V_nO_{2n-1} , $Ti_{n-2}Cr_2O_{2n-1}$. *Ark Kemi* 21:413
- [17] Horiuchi H, Morimoto N, Tokonami M (1976) Crystal structures of V_nO_{2n-1} ($2 \leq n \leq 7$). *J Sol Stat Chem* 17:407. [https://doi.org/10.1016/S0022-4596\(76\)80011-4](https://doi.org/10.1016/S0022-4596(76)80011-4)
- [18] Surnev S, Kresse G, Ramsey MG, Netzer FP (2001) Novel interface-mediated metastable oxide phases: vanadium oxides on Pd(111). *J Am Chem Soc* 87:086102-2. <https://doi.org/10.1103/PhysRevLett.87.086102>
- [19] Window AJ, Hentz A, Sheppard DC, Parkinson GS, Niehus H, Ahlbehrendt D, Noakes TCQ, Bailey P, Woodruff DP (2011) V_2O_3 (0001) surface termination: phase equilibrium. *Phys Rev Lett* 107:016105. <https://doi.org/10.1103/PhysRevLett.107.016105>
- [20] Okinaka H, Nagasawa K, Kosuge K, Bando Y, Kachi S, Takada T (1970) Electrical properties of V_6O_{11} and V_7O_{13} single crystals. *J Phys Soc Jpn* 29:245. <https://doi.org/10.1143/JPSJ.29.245>
- [21] Ueda Y, Kosuge K, Kachi S (1980) Phase diagram and some physical properties of $V_2O_3 + x$ ($0 \leq x \leq 0.080$). *J Sol Stat Chem* 31:171. [https://doi.org/10.1016/0022-4596\(80\)90019-5](https://doi.org/10.1016/0022-4596(80)90019-5)
- [22] Dubey P, Kaurav N, Devan RS, Okram GS, Kuo YK (2018) The effect of stoichiometry on the structural, thermal and electronic properties of thermally decomposed nickel oxide. *RSC Adv* 8:5882. <https://doi.org/10.1039/C8RA00157J>
- [23] Okamoto H (1997) Cr–O (chromium–oxygen). *J Phase Equilib* 18:402. <https://doi.org/10.1007/s11669-997-0072-0>
- [24] McWhan DB, Remeika JP (1970) Metal-insulator transition in $(V_{1-x}Cr_x)_2O_3$. *Phys Rev B* 2:3734. <https://doi.org/10.1103/PhysRevB.2.3734>

Publisher's Note Springer Nature remains neutral with regard to jurisdictional claims in published maps and institutional affiliations.